Light scattering properties of spheroidal particles

Shoji Asano

Light scattering characteristics of spheroidal particles are studied for a wide range of particle parameters and orientations. The method of computation is based on the scattering theory for a homogeneous spheroid developed by us, and the calculation is extended to fairly large spheroidal particles of a size parameter up to 30. Effects of the particle size, shape, index of refraction, and orientation on the scattering efficiency factors and the scattering intensity functions are investigated and interpreted physically. The scattering properties of prolate and oblate spheroids with incidence parallel to the rotation axis constitute the extremes. The prolate spheroids at parallel incidence have steep and high resonance maxima in the scattering efficiency factors and broad and low forwardscattering peaks in the intensity functions; on the other hand, the oblate spheroids at parallel incidence have broad and low resonance maxima and sharp and high forwardscattering peaks. With an increase of the incidence angle, the scattering behavior of prolate spheroids approaches that of oblate spheroids at parallel incidence and vice versa. It is shown that, for oblique incidence, the scattering properties of a long slender prolate spheroid resemble those of an infinitely long circular cylinder. Effects of absorption on the extinction efficiency factors and scattering intensity functions are examined. Some problems in numerical calculation of the spheroidal wave functions and the infinite series solutions are discussed.

I. Introduction

Currently there is great progress being made in the theoretical study of light scattering by nonspherical particles of finite size. One of the powerful techniques for analyzing the scattering of electromagnetic waves by nonspherical particles is the integral equation formulation of the scattering problem. Several ways of solving the integral equations have been proposed, and the method has been widely applied to the axisymmetric bodies such as spheroids,[1–6] circular disks,[7] finite rods,[1,8] and infinite cylinders[6,9,10] with various cross-sectional shapes. The method gives exact solutions; however, it requires substantial numerical integrations over the surface or volume of the scattering body.

Another method for analyzing the scattering by spheroids has been developed by Asano and Yamamoto.[11] This method is the separation of variables for the vector wave equations in the spheroidal coordinate system. This gives the exact quasi-analytic solution for light scattering by homogeneous isotropic spheroids. The computations are straightforward. The electromagnetic field vectors are expanded in terms of the spheroidal vector wave functions. The unknown coefficients of expansion are determined by a system of linear equations derived from the boundary conditions. The solutions for the prolate and oblate spheroidal systems are in the same form.

In the previous paper,[11] we examined the light scattering properties of relatively small spheroids with the real index of refraction $\tilde{m} = 1.33$. In this paper, we shall discuss scattering characteristics such as the efficiency factors for scattering and absorption, the forwardscattering and backscattering, and the angular distributions of scattered intensity for various sizes, eccentricities, complex refractive indexes, and orientations of the spheroids. Computations are extended to fairly large particle sizes. The method of calculation and the notation are the same as those in Ref. 11.

II. Scattering Geometry

The light scattering by a spheroidal particle is specified by the following five physical quantities: (1) particle size relative to the wavelength of incident wave; (2) eccentricity; (3) complex refractive index $\tilde{m}$ relative to that of the surrounding medium; (4) orientation of particle to the incident wave; and (5) the observation direction.

We shall define, in this paper, the particle size parameter α by

$$\alpha = 2\pi a/\lambda, \tag{1}$$

where a is the semimajor axis of the ellipse, and λ is the wavelength of the incident wave. We specify the shape of the spheroid by the ratio a/b of the semimajor axis

The author is with NASA Goddard Space Flight Center, Institute for Space Studies, New York, New York 10025.

Received 27 September 1978.
0003-6935/79/050712-12$00.50/0.

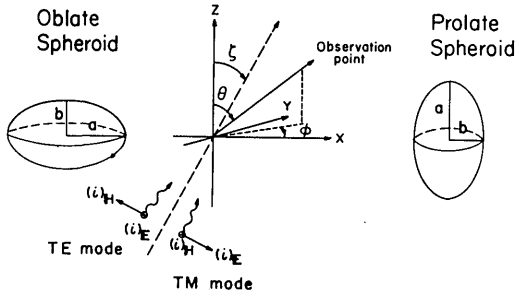

Fig. 1. Scattering geometry. The spherical coordinate system is adopted to represent the scattered field in the far-field zone. The origin of the coordinate system and the z axis are the center and the axis of revolution of the spheroid, respectively. The angle of incidence ζ is the angle in the plane of incidence (the x–z plane) between the direction of incidence and the z axis.

a to the semiminor axis b, which has a value greater than unity. We prefer the ratio a/b rather than the eccentricity as a more direct measure of the elongation of the spheroid.

Figure 1 shows the geometry of scattering of a linearly polarized plane electromagnetic wave incident at an angle ζ to the z axis. The origin of the coordinate system should be taken at the center of the spheroid with the z axis as the axis of rotation, i.e., as the major axis for a prolate spheroid, and the minor axis for an oblate one. The spherical coordinate system (θ,ϕ) is adopted to represent the direction of a far-field observation point, where θ is the zenith angle measured from the positive z axis, and ϕ is the azimuth angle. The direction of incidence is assumed to be in the $\phi = 0$ plane (x–z plane) and is thus identified by $(\zeta,0)$.

For oblique incidence ($\zeta \neq 0$) the incident wave can be resolved into two polarization components, the TE and TM modes, for which the electric and magnetic vectors, respectively, vibrate perpendicularly to the plane of incidence. For $\zeta \neq 0$, therefore, we have to consider the two polarization cases separately. For incidence parallel to the rotation axis ($\zeta = 0$), however, the two cases give identical results due to the symmetry with respect to the incident wave.

III. Numerical Calculations

A. Spheroidal Wave Functions

In our theory, solutions are expressed in terms of the spheroidal wave functions.[12] The spheroidal wave functions are important functions in many fields of physics, especially in the fields of acoustics and electromagnetic theory. At present, however, their use is severely limited due to the absence of extensive numerical tables and due to computational instabilities for large values of the parameters. The spheroidal wave functions are functions not only of a coordinate argument but also of a physical parameter $c = 2\pi l/\lambda$. Here, l is the semifocal distance of the ellipse. Numerical values[13–17] published until now have been only for small spheroids with $c \lesssim 10$.

Difficulties arise particularly in calculation of the radial functions of the second kind for large c and large a/b. The series representation of the functions in terms of spherical Neumann functions [Flammer[12] (4·1·19)] converges slowly. For the prolate radial functions of the second kind, some improvement of convergence of the series has been made by Sinha and MacPhie[18] using an integral approximation for $c < 9$.

Another expansion of the radial functions of the second kind of degree n and order m, in terms of the associated Legendre functions [Flammer (4·2·6)–(4·2·7)] loses its accuracy for small values of the difference $(n - m)$ as c becomes large. In addition, for the prolate radial functions, the factor

$$\sum_{r=0,1}^{\infty}{}' \frac{(2m+r)!}{r!} d_r^{mn}(c)$$

becomes very small, approaching zero for large c as $(n - m) \to 0$ and/or $m \to 0$ due to cancellation of terms; the factor is involved in the series representation of the radial functions.

We find that expansion of oblate radial functions of the third kind $R_{mn}^{(3)}(-ic;i\xi)$ in terms of the associated Legendre functions of the second kind [Flammer (4·5·4)] gives good results for the radial functions of the second kind $R_{mn}^{(2)}(-ic;i\xi)$, especially for small $(n - m)$ and even for large c through the relation

$$R_{mn}^{(2)}(-ic;i\xi) = \frac{1}{i}\left[R_{mn}^{(3)}(-ic;i\xi) - R_{mn}^{(1)}(-ic;i\xi)\right], \qquad (2)$$

where $R_{mn}^{(1)}(-ic;i\xi)$ is the oblate radial function of the first kind and can be calculated easily by series expansion in terms of the spherical Bessel functions [Flammer (4·1·15)]. This method has been used by Hanish *et al.*[15,16] in their tabulation of the oblate radial functions for small $c \leq 8$.

By adopting different computational methods and choosing the best methods, we have extended calculations of the spheroidal radial functions to large sizes, up to $c \sim 35$. The eigenvalues were evaluated by means of Bouwkamp's[19] correction scheme using a starting value estimated with the matrix method of Hodge.[20]

B. Convergence of Solutions

Solutions for scattering by spheroids are expressed as infinite double-summation series over m and n for oblique incidence and as infinite summation series over only n with $m = 1$ for parallel incidence. Practically, the infinite series are truncated to finite series including only the first M terms for the summation over m and N terms for the summation over n. M and N are determined by repeating calculations for successively larger values of M and N, until the final results converge to a specified accuracy. We have imposed a convergence condition of more than four-digit accuracy.

Maximum values of M and N depend, of course, on the particle parameters and orientations. Dependence of N on the size α and on the shape a/b has been discussed in some detail in Ref. 11. A small spheroid with small a/b and small $\tilde{m}$ takes a small value of N, while a large spheroid with large a/b and large $\tilde{m}$ requires a much larger N.

An example of convergence behavior of the summa-

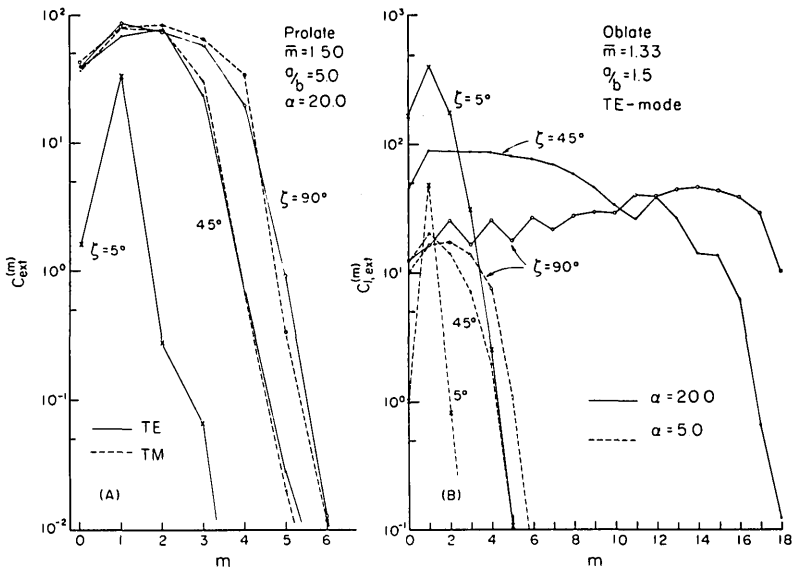

Fig. 2. (a) Value of the mth term of the infinite summation series, Eq. (3), for the extinction cross sections with oblique incidence of the TE (solid lines) and TM (broken lines) mode polarization waves for the prolate spheroid with $\tilde{m} = 1.50$, $a/b = 5$, and $\alpha = 20$. (b) Value of the mth term of the infinite summation series, Eq. (3), for oblate spheroids with $\tilde{m} = 1.33$, $a/b = 1.5$, and $\alpha = 5$ (broken lines) and $\alpha = 20$ (solid lines) for oblique incidence of the TE mode polarization wave.

tion series over m (ϕ dependence) is shown in Figs. 2(a) and 2(b). The mth term of the series for the extinction cross section [Ref. 11, Eqs. (110) and (111)]

$$C_{2,\mathrm{ext}}^{(m)} = -\mathrm{Re} \sum_{n=m}^{N} [\alpha_{2}^{1,mn} \sigma_{mn}(\zeta) + \beta_{2}^{1,mn} \chi_{mn}(\zeta)] \tag{3}$$

is plotted against order m. Figure 2(a) is for a large slender prolate spheroid with $\alpha = 20$, $a/b = 5$, and $\tilde{m} = 1.50$ for the two polarization modes of TE and TM at the three incidence angles $\zeta = 5°$, 45°, and 90°. This figure shows that convergence of the m series is slower for larger incidence angles and that, for the small incidence angle of $\zeta = 5°$, the term with $m = 1$ dominates. This means that a larger incidence angle requires a larger M for the Fourier series expansion in ϕ of the azimuth-dependent scattered field. These results are due to the fact that, at a fixed zenith angle θ variation of the scattering angle Θ as a function of a change of the azimuth angle ϕ becomes larger with a larger ζ through the relation

$$\cos\Theta = \cos\zeta \cdot \cos\theta + \sin\zeta \cdot \sin\theta \cdot \cos\phi, \tag{4}$$

and thus the anisotropy of the scattered field increases. At $\zeta = 90°$, a change of ϕ in the $\theta = 90°$ plane (the x–y plane) corresponds exactly to a change of the scattering angle. At $\zeta = 0°$ (parallel incidence), only a single term with $m = 1$ appears; that is, the ϕ dependence of the scattered field is $\sin\phi$ or $\cos\phi$. Figure 2(b) is for oblate spheroids with $\tilde{m} = 1.33$, $a/b = 1.5$, two different sizes $\alpha = 5$ and 20, and incidence of the TE mode polarization wave. Naturally, convergence is much more rapid for the small oblate spheroid ($\alpha = 5$) than for the large one ($\alpha = 20$). Compared with Fig. 2(a), convergence is much slower for the slightly nonspherical oblate spheroid of $a/b = 1.5$ than for the slender prolate spheroid of $a/b = 5$ with the same size parameter $\alpha = 20$.

In general, for a given size the spheroids with smaller a/b require a larger value of m, especially for prolate spheroids. This is related to the increased anisotropy of the scattered field with respect to ϕ, which occurs with the increase of the volume and geometrical cross-sectional area of the spheroids for smaller a/b but fixed α. In addition, the oblate spheroids require somewhat larger values of M and N than are required for the prolate spheroids with the same α and a/b. This is a result of the fact that, for the same α and a/b, the oblate spheroids have larger volume and geometrical cross-sectional area than prolate spheroids.

For large spheroids (e.g., $\alpha \gtrsim 17$ for prolate spheroids with $a/b = 2$ and $\tilde{m} = 1.50$), a numerical instability occurs in the calculation of the $m = 0$ term at oblique incidence $0° < \zeta < 90°$. When erroneous results were generated for the $m = 0$ term, we found that the coefficient matrix of the system of linear equations, which determine the unknown scattering coefficients $\beta_{0,2p}$ ($p = 0,1,2\ldots$), was ill-conditioned with respect to matrix calculations, while the system of linear equations for the odd-ordered coefficients $\beta_{0,2p+1}$($p = 0,1,2\ldots$) was still very stable. [It has been shown that the even-ordered coefficients and the odd-ordered ones can be decoupled and thus determined separately and that, for $m = 0$, other coefficients α_{0n}($n = 0,1,2\ldots$) are always zero because $f_{0n}(\zeta) = 0$.][11] Ill-conditioning means that solutions of the system of linear equations are sensitive to small changes of the coefficients in the equations. This ill-conditioning starts at a smaller size α for a spheroid with smaller a/b. A cause of the ill-conditioning may be insufficient accuracy in the numerical computations, although all calculations were carried out with double precision arithmetic (fifteen significant figures). A similar instability has been reported by Barber[2] in his application of the extended boundary condition method to scattering by absorbing spheroids.

These instabilities in the numerical computations prevented the extension of the computations to larger spheroids than those considered in this paper.

IV. Scattering Efficiency Factors

A. Parallel Incidence ($\zeta = 0$)

The efficiency factor for scattering Q_{sca} is defined here by the ratio of the scattering cross section C_{sca} to the area of the geometrical shadow of the spheroid $G(\zeta)$ at the incidence angle ζ. For nonabsorbing particles with real refractive indexes, the scattering efficiency is equal to the extinction efficiency. At the parallel incidence $\zeta = 0$, the scattering cross sections for the TE and TM mode linear polarizations of the incident wave are identical and are given by Eq. (119) in Ref. 11. The geometrical shadow areas $G(\zeta)$ are given by

$$G(\zeta) = \pi b(a^2 \sin^2\zeta + b^2 \cos^2\zeta)^{1/2}, \quad (5)$$

for the prolate spheroids and by

$$G(\zeta) = \pi a(b^2 \sin^2\zeta + a^2 \cos^2\zeta)^{1/2} \quad (6)$$

for the oblate spheroids. They become πb^2 and πa^2, respectively, at $\zeta = 0°$.

In Fig. 3, the scattering efficiency factors Q_{sca} of the prolate spheroids with $\tilde{m} = 1.50$ are plotted as a function of the size parameter α for various values of the shape parameter from $a/b = 1.5$ to 5. Computation was performed with resolution in size parameter of 0.5 for $a/b \geqq 2$ and 0.25 for $a/b \leqq 1.5$. For small prolate spheroids, $\alpha < 4.0$, the scattering efficiency factors are greater for the spheroids that are closer to being spheres, i.e., for the smaller a/b. $Q_{sca}(\alpha)$ for $a/b = 1.5$ is similar to that for spheres with oscillations which damp out for large size parameters as Q_{sca} approaches the geometrical optics limit of 2. A striking feature is that, with increase of a/b, the first resonance maximum occurs at large size parameter and the peak value increases.

The major maxima and minima in Fig. 3 are due to interference of light diffracted with light transmitted by the particle. The phase shift for a light ray passing through the particle along the axis in the direction of incidence is $\rho = 2\alpha(\tilde{m} - 1)$, which equals α or $2\pi a/\lambda$ for

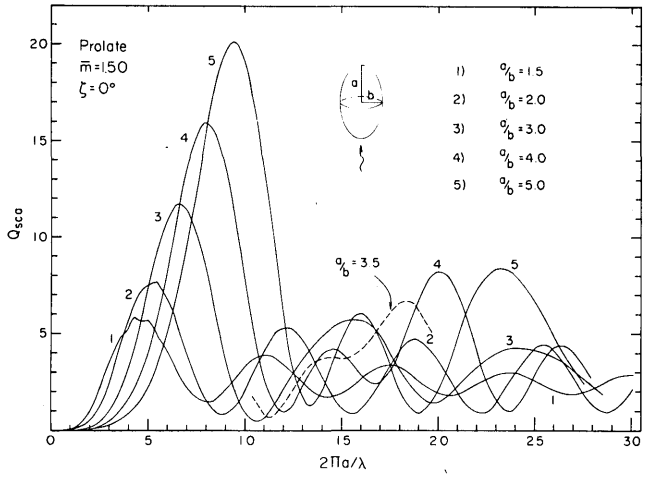

Fig. 3. Scattering efficiency factors Q_{sca} at $\zeta = 0°$ as a function of the size parameter $2\pi a/\lambda$ for the prolate spheroids with $\tilde{m} = 1.50$ for several values of the shape parameter a/b.

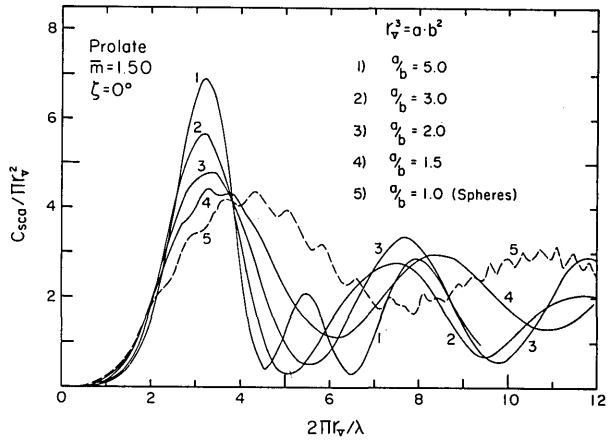

Fig. 4. Scattering cross sections of prolate spheroids normalized by the area πr_v^2 of a sphere of the same volume as a function of the size parameter of the sphere $2\pi r_v/\lambda$ for prolate spheroids with $\tilde{m} = 1.50$ and $a/b = 1.5$ 2, 3, and 5. The curve for spheres is shown by the dotted line.

the case $\tilde{m} = 1.5$. Thus successive maxima, caused by constructive interference, occur at intervals of $\sim 2\pi$. The case $a/b = 3$ is a notable exception, however, the average separation of the maxima would also be $\sim 2\pi$ if there were one additional maximum. The results for $a/b = 3.5$ shown by the dashed curve, in fact, suggest that the expected second and third maxima have somehow combined into a single maximum for $a/b \sim 3$.

Application of the anomalous diffraction approximation of van de Hulst[21] to scattering by prolate spheroids at the parallel incidence will give extinction efficiency curves identical to those of spheres, without regard to a/b but with the phase lag parameter $\rho = 2\alpha(\tilde{m} - 1)$. However, in fact, the position and peak value of the first maximum of the scattering efficiency curves in Fig.3 are strongly dependent on a/b. Furthermore, the mean periods of the major oscillations of the scattering efficiency curves are a little larger for the prolate spheroids than for spheres. These discrepancies from the expectation of the approximation of anomalous diffraction can be attributed to effects of edge phenomena or grazing reflection.[21] The edge phenomena depend on the curvature of the profile of the scattering body at the edge; the profile is perpendicular to the wavefront of the incident wave. The radius of curvature is $R = a^2/b$ for the prolate spheroid at parallel incidence. This means a larger radius of curvature and, therefore, a larger contribution of edge phenomena for prolate spheroids with larger a/b but the same a.

The scattering cross sections of the prolate spheroids are replotted in Fig. 4 as a function of the size parameter $2\pi r_v/\lambda$ for spheres of the same volume; here r_v is the radius of the sphere, i.e., $r_v^3 = ab^2$. The scattering cross sections are normalized by the cross-sectional area πr_v^2 of the sphere. In the figure, as a reference, the scattering efficiency curve of spheres is also shown. The scattering efficiency factors of spheres were computed

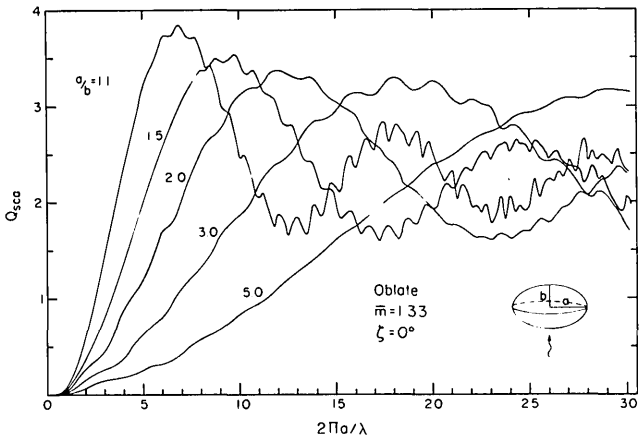

Fig. 5. Scattering efficiency factors Q_{sca} at $\zeta = 0°$ as a function of the size parameter $2\pi a/\lambda$ for oblate spheroids with $\tilde{m} = 1.33$ and $a/b = 1.1$, 1.5, 2, 3, and 5.

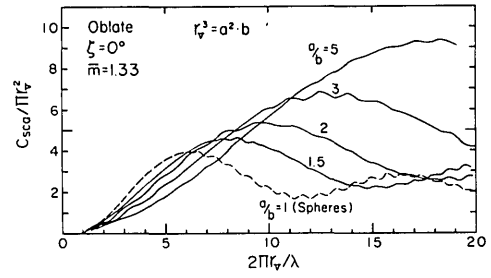

Fig. 6. Scattering cross sections of oblate spheroids normalized by the area πr_v^2 of a sphere of the same volume as a function of the size parameter of the sphere $2\pi r_v/\lambda$ for oblate spheroids with $\tilde{m} = 1.33$ and $a/b = 1.5$, 2, 3, and 5. The curve for spheres is shown by the dotted line.

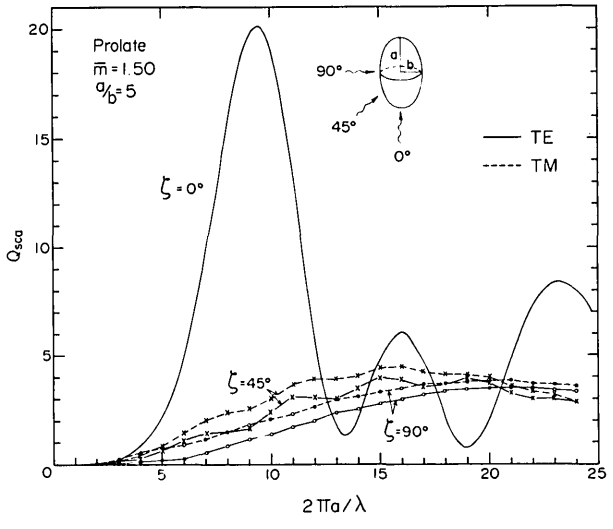

Fig. 7. Scattering efficiency factors Q_{sca} as a function of the size parameter $2\pi a/\lambda$ for prolate spheroids with $\tilde{m} = 1.50$ and $a/b = 5$ for incidence of the TE (solid lines) and TM (broken lines) mode polarization waves at incidence angles $\zeta = 0°$, 45°, and 90°.

from the Mie theory with a size resolution of 0.2. The figure shows a change of scattering efficiency curves with increase of a/b: the curve is as a whole shifted to smaller values of $2\pi r_v/\lambda$, and the first maxima become sharper and higher. An evident feature is the damping of the ripplelike fluctuations superimposed on the major oscillations of the scattering efficiency curves. For slender spheroids ($a/b > 2$), the ripples are completely washed out, and the profiles of the scattering efficiency curves are greatly different from that for spheres. It is interesting that the first maxima of the scattering efficiency curves of slender prolate spheroids at $\zeta = 0°$ occur at similar volumes.

Figure 5 illustrates scattering efficiency curves of oblate spheroids with $\tilde{m} = 1.33$ at $\zeta = 0°$ as a function of the size parameter α for various values of a/b. With increase of a/b, the first resonance maximum becomes broader and lower, and its position is shifted to larger sizes. However, the decrease of the peak heights is less striking than the increase for prolate spheroids shown in Fig. 3. Regarding the position of the first maximum, if the scattering efficiency factors are plotted against the phase shift parameter $\rho = 4\pi b/\lambda \cdot (\tilde{m} - 1)$ instead of α, the first maximum occurs near $\rho = 4.1$, which is in good agreement with the position of the first maximum of the extinction efficiency curve for spheres with $\tilde{m} = 1.33$. This suggests a less important contribution of edge phenomena to the scattering by oblate spheroids at $\zeta = 0°$ due to the smaller radius of curvature of the profile at the edge $R = b^2/a$ than for prolate spheroids. Another striking feature of the scattering efficiency curves of the oblate spheroids is that the ripples superimposed on the major oscillations still remain even for thin oblate spheroids of $a/b = 5$, although the amplitude of ripples is much reduced. With the increase of a/b, the period of the ripples is increased from 0.8 in α for $a/b = 1.1$ to 2.0 for $a/b = 3$.

In Fig. 6, the scattering cross sections of the oblate spheroids are replotted against the size parameter $2\pi r_v/\lambda$ for spheres of the same volume, here $r_v^3 = a^2 b$. The curves of the scattering cross sections normalized by πr_v^2 are greatly different from those for spheres, showing increasing first major maxima at larger sizes with increase of a/b. For small sizes $2\pi r_v/\lambda \leq 6$, the spheres scatter more radiation than the oblate spheroids of equal volume, but, for larger sizes, the oblate spheroids scatter more radiation than spheres of the same volume because of their greater geometrical cross section πa^2.

B. Oblique Incidence ($\zeta \neq 0$)

Figure 7 shows the scattering efficiency factors of prolate spheroids with $\tilde{m} = 1.50$ and $a/b = 5$ as a function of the size parameter α for three incidence angles $\zeta = 0°$, 45°, and 90°. The computed values are connected by straight line segments because of the coarse computational resolution of 1.0 in α for oblique incidences. For increasing obliquity the first major maxima are drastically shifted in position and in profile from the case of parallel incidence $\zeta = 0°$. In this size range, the scattering efficiency factors for the TM mode po-

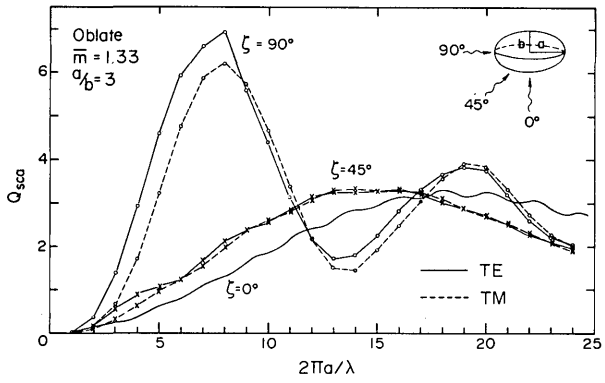

Fig. 8. Scattering efficiency factors Q_{sca} as a function of the size parameter $2\pi a/\lambda$ for oblate spheroids with $\tilde{m} = 1.33$ and $a/b = 3$ for incidence of the TE (solid lines) and TM (broken lines) mode polarization waves at incidence angles $\zeta = 0°$, 45°, and 90°.

larization are greater than those for the TE mode polarization, although the difference between the two polarization cases decreases with increase of α, since in the geometric optics limit they would coincide.

The change in profile of the scattering efficiency curves of prolate spheroids as the incidence angle changes is fairly similar, except for the change in magnitude to that of infinite cylinders[22] at oblique incidence. For instance, a broad and rippled first resonance maximum at normal incidence to the cylinder shifts to sharp and smooth one at grazing incidence, where our $\zeta = 90°$ incidence corresponds to normal incidence to the cylinder and our $\zeta \to 0°$ corresponds to the grazing incidence.

The corresponding figure for oblate spheroids with $\tilde{m} = 1.33$ and $a/b = 3$ is given in Fig. 8. The behavior of these curves with change of ζ is opposite to that of prolate spheroids, as would be expected from the qualitative similarity of the prolate spheroid shape at $\zeta = 90°$ to the oblate spheroid shape at $\zeta = 0°$ and vice versa. With the increase of ζ, the scattering efficiency curves are shifted as a whole to smaller sizes, with the major oscillations having larger amplitudes and shorter periods—the first maxima become steeper and smoother with higher peaks occurring at smaller sizes. For sizes larger than the size at the first major maxima, the curves for the TE and TM mode polarizations cross one another several times systematically, especially at $\zeta = 90°$. Similar crossing phenomena of the scattering efficiency curves for the different polarizations have been reported for the scattering by obliquely oriented infinite circular cylinders[22] and for the microwave scattering by prolate spheroidal particles.[23]

In summary, for spheroids with a given shape parameter, the scattering efficiency curves have steeper and higher maxima with shorter periods of the major oscillations occurring for the direction of incidence for which the geometrical shadow area $G(\zeta)$ of the spheroid is smaller or the pathlength through the center of the spheroid is longer, i.e., $\zeta \to 0°$ for the prolate spheroid and $\zeta \to 90°$ for the oblate spheroid; they have broader and lower rippled maxima at the incidence for which $G(\zeta)$ becomes larger or the pathlength becomes shorter, i.e., $\zeta \to 90°$ for the prolate spheroid and $\zeta \to 0°$ for the oblate spheroid.

The broad maxima of the scattering efficiency curves are due to the superposition of many resonance peaks, each associated with a partial wave,[24] so the broad maxima tend to have a ripple structure. The ripple structure of the scattering efficiency curves of spheres has been extensively studied in relation to the glory phenomena or the strong enhancement in the backscattering by spheres.[21,24–29] The ripples and the rapid oscillations in the backscattering are caused by the effects of surface waves excited by the incident rays tangential to a sphere. The ripples are due to interference between the diffracted waves and surface waves. Several models of the surface wave effects on the rapidly varying quasi-periodic fluctuations in the backscattering by spheres have been proposed.[21,25,27] We have found similar ripple structures in the scattering efficiency curves of the spheroids. But the appearance of the phenomena is dependent not only on size and shape but also on the orientation of the spheroids.

V. Forwardscattering and Backscattering

Because of the special interest in applications to particle measurements by lidar and radar, the backscattering properties of spheroidal particles will be discussed briefly. The forwardscattering is also examined in relation to the extinction or scattering efficiency factors of the spheroids.

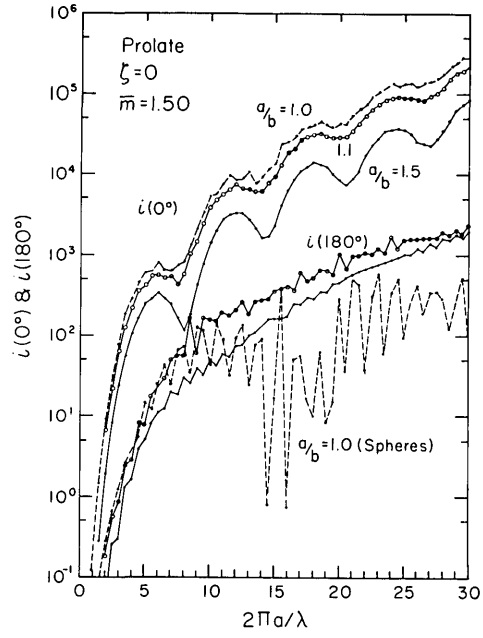

Fig. 9. Intensity functions of forwardscattering $i(0°)$ and backscattering $i(180°)$ at parallel incidence as a function of the size parameter $2\pi a/\lambda$ for the slightly nonspherical prolate spheroids with $\tilde{m} = 1.50$ and $a/b = 1.1$ and 1.5. The intensity functions for spheres are shown by dotted lines.

The intensity functions at oblique incidence are given by Eqs. (102)–(105) in Ref. 11, setting $(\zeta,0°)$ and $(180° - \zeta, 180°)$ in the angular coordinates (θ,ϕ) for the forwardscattering and backscattering, respectively. From the expression for the intensity functions, it follows that there is no cross polarization, i.e., $i_{12} = i_{21} = 0$ in the plane of incidence, i.e., the $\phi = 0°$ and 180° plane.[30] Thus for oblique incidence of unpolarized light, the intensity functions of the forwardscattering and backscattering are given, respectively, by

$$i(\zeta,0°) = \tfrac{1}{2}[i_{11}(\zeta,0°) + i_{22}(\zeta,0°)], \tag{7}$$

$$i(180° - \zeta, 180°) = \tfrac{1}{2}[i_{11}(180° - \zeta, 180°) + i_{22}(180° - \zeta, 180°)]. \tag{8}$$

At parallel incidence ($\zeta = 0°$), the intensity functions [Eqs. (107) and (108) in Ref. 11] become

$$i_1(0°) = i_2(0°) = \left|\sum_{n=1}^{\infty}\left[\sum_{r=0,1}^{\infty}{}' \frac{(r+1)(r+2)}{2} d_r^{\ln}\right](\alpha_{\ln} + \beta_{\ln})\right|^2, \tag{9}$$

$$i_1(180°) = i_2(180°) = \left|\sum_{n=1}^{\infty}\left[\sum_{r=0,1}^{\infty}{}' \frac{(r+1)(r+2)}{2} d_r^{\ln}\right](-1)^n(\alpha_{\ln} - \beta_{\ln})\right|^2, \tag{10}$$

for forwardscattering and backscattering, respectively.

Figure 9 shows the forwardscattering and backscattering intensity functions of prolate spheroids with $a/b = 1.1$ and 1.5 as a function of the size parameter α at parallel incidence. The intensity functions of spheres are also plotted; the plotting resolution in this figure is 0.5 in the size parameter. The figure demonstrates the gradual change of scattering by slightly nonspherical prolate spheroids from scattering by spheres. At a given size, the forwardscattering intensity is smaller for the prolate spheroids with larger a/b because of their smaller shadow area $G(0°)$; for large particles, the forwardscattering is mostly contributed by the diffracted light. The curves of the forwardscattering intensity oscillate with a larger amplitude for larger a/b. The oscillations correspond to the major oscillations of the scattering efficiency curves, and they are due to interference of the diffracted and transmitted light. The positions of maxima of the forwardscattering intensity curves are slightly shifted to larger sizes than those of the scattering efficiency curves, although minima of both curves are in phase.

The backscattering intensity of spheres fluctuates sharply due to the effects of surface waves. The effects of surface waves are more prominent for the backscattering than for the forwardscattering, because of the greater contribution of diffracted light to the forwardscattering.[31] For the slightly nonspherical prolate spheroids, the fluctuation is damped greatly, and the curves become smoother. For large sizes, $\alpha > 13$, the backscattering by the prolate spheroids is larger than that by spheres in spite of the smaller shadow area of the prolate spheroids. For slender prolate spheroids, naturally, the backscattering becomes much less than that of spheres, and it begins to oscillate periodically as shown in Fig. 10.

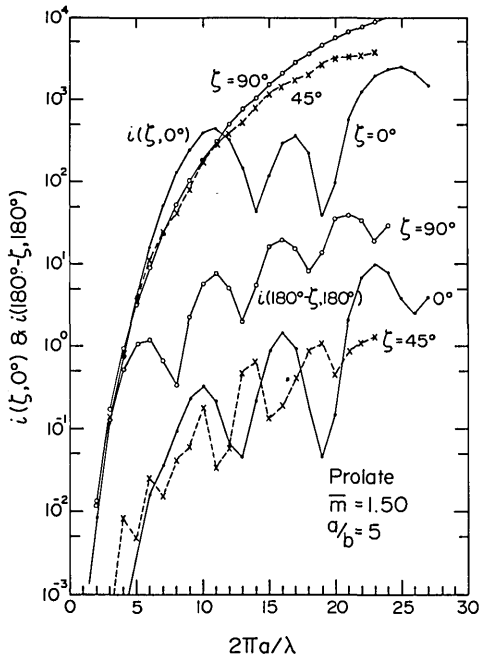

Fig. 10. Intensity functions of forwardscattering $i(\zeta,0°)$ and backscattering $i(180° - \zeta, 180°)$ for unpolarized incident light at $\zeta = 0°$, 45°, and 90° as a function of the size parameter $2\pi a/\lambda$ for prolate spheroids with $\bar{m} = 1.50$ and $a/b = 5$.

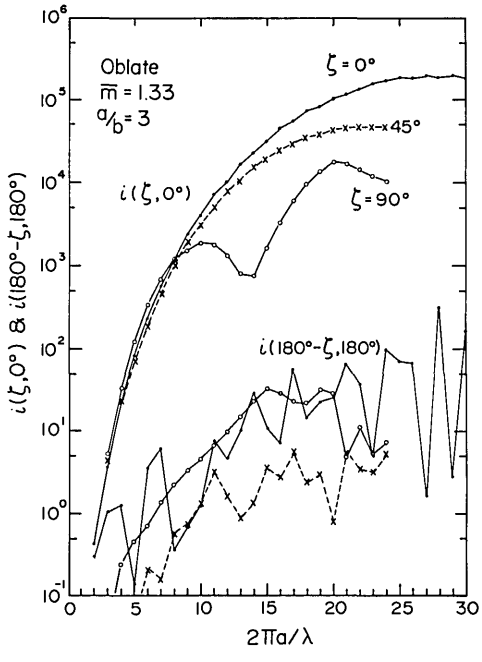

Fig. 11. Intensity functions of forwardscattering $i(\zeta,0°)$ and backscattering $i(180° - \zeta, 180°)$ for unpolarized incident light at $\zeta = 0°$, 45°, and 90° as a function of the size parameter $2\pi a/\lambda$ for oblate spheroids with $\bar{m} = 1.33$ and $a/b = 3$.

Figure 10 illustrates the forwardscattering and backscattering intensity functions of the slender prolate spheroids with $\tilde{m} = 1.50$ and $a/b = 5$ for incidence of unpolarized light at $\zeta = 0°$, 45°, and 90°. Oscillations corresponding to those of the scattering efficiency curves in Fig. 7 are clearly seen on the forwardscattering curves, especially at $\zeta = 0°$. For large sizes, $\alpha > 11$, the forwardscattering intensity is larger for larger incidence angles because of the greater shadow areas, while for small sizes, $\alpha < 5$, it is nearly independent of the incidence angle. The backscattering intensity functions at $\zeta = 0°$ and 90° oscillate periodically. This smooth periodic oscillation may be due to interference of the axial rays reflected from front and rear surfaces and of the glory rays emerging in the backward direction after internal reflections.[24] At $\zeta = 45°$, the oscillation of the backscattering curve is rather irregular, and its mean values are almost the same as those of $\zeta = 0°$ in spite of the greater shadow area—$G(45°) > G(0°)$—because of the lack of backward reflection of axial rays from the front surfaces due to the asymmetric orientation to the incident direction.

Similar figures for oblate spheroids with $\tilde{m} = 1.33$ and $a/b = 3$ are given in Fig. 11. This figure should be referred to Fig. 8; the general features of the forwardscattering curves are similar to those of the scattering efficiency curves. In contrast with the prolate spheroids for large sizes, $\alpha > 8$, the forwardscattering intensity becomes smaller for a larger incidence angle because of the smaller shadow area. But for small sizes, $\alpha < 8$, the forwardscattering intensity at $\zeta = 90°$ is a little larger than at $\zeta = 0°$. The backscattering intensity curves show irregular fluctuations; the amplitude of fluctuations decreases with increase of ζ. This feature corresponds to the damping of the ripplelike fluctuations on the scattering efficiency curves in Fig. 8.

For incidence of polarized light, the difference of the forwardscattering intensities for the TE and TM mode polarizations has the same sign as that of the scattering efficiency factors for the different polarizations. For backscattering, however, opposite signs occur for some sizes.

VI. Angular Distribution of Scattered Intensity

Figure 12 shows the angular distribution of the intensity functions for incidence of unpolarized light $i(\theta,\phi)$ of the prolate spheroids with $\tilde{m} = 1.50$, $a/b = 5$, and $\alpha = 10$ at incidence angles $\zeta = 0°$, 45°, and 90°. The figure displays the distribution of the intensity functions on the plane of incidence, i.e., the $\phi = 0°$ and 180° plane as a function of the zenith angle θ. As mentioned before, there is no cross polarization or depolarization on this plane. The angular patterns at $\zeta = 0°$ and 90° are, of course, symmetrical with respect to the incident direction $(\zeta,0°)$. On the other hand, the profile at $\zeta = 45°$ is not symmetrical, because of the asymmetric orientation of the spheroid with respect to the incident direction. The forwardscattering peak at $\zeta = 0°$ is larger than it is at $\zeta = 45°$ and 90° in spite of the smallest shadow area at $\zeta = 0°$. This peak corresponds to the strong first resonance maximum of the scattering efficiency curve at $\zeta = 0°$ around this size (Figs. 7 and 10).

Corresponding figures for the intensity functions $i(\theta,\phi)$ of the oblate spheroid with $\tilde{m} = 1.33$, $a/b = 3$, and $\alpha = 10$ are given in Fig. 13. The variation of the intensity function profiles with incidence angle is again opposite to that for prolate spheroids. With increase of ζ, the forwardscattering peak becomes lower and broader, and the number of maxima and minima of the oscillation increases. At $\zeta = 45°$, the distribution of the intensity function is asymmetrical with respect to the incidence direction, and it varies more slowly, having a large second maximum around (110°, 0°) on the right half-plane divided by the incidence direction.

Figure 14 illustrates the angular distribution of the intensity functions $i(\theta,\phi)$ for the large slender prolate spheroid with $\tilde{m} = 1.50$, $a/b = 5$, and $\alpha = 20$ at $\zeta = 45°$ as a function of θ on three scattering planes through the z axis: one parallel to the incidence plane ($\phi = 0°$ and

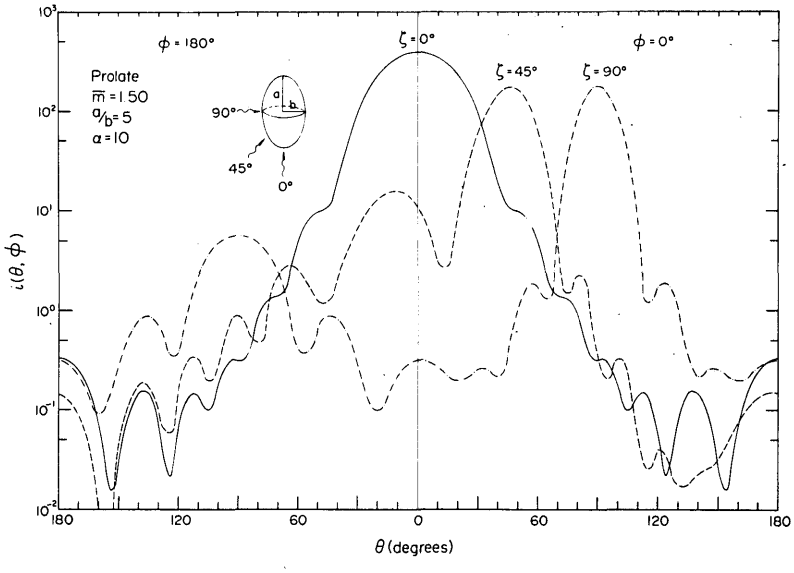

Fig. 12. Angular distribution of the intensity functions $i(\theta,\phi)$ for unpolarized incident light as a function of the zenith angle θ on the incidence plane ($\phi = 0° - 180°$) for the prolate spheroid with $\tilde{m} = 1.50$, $a/b = 5$, and $\alpha = 10$ at incidence angles $\theta = 0°$, 45°, and 90°.

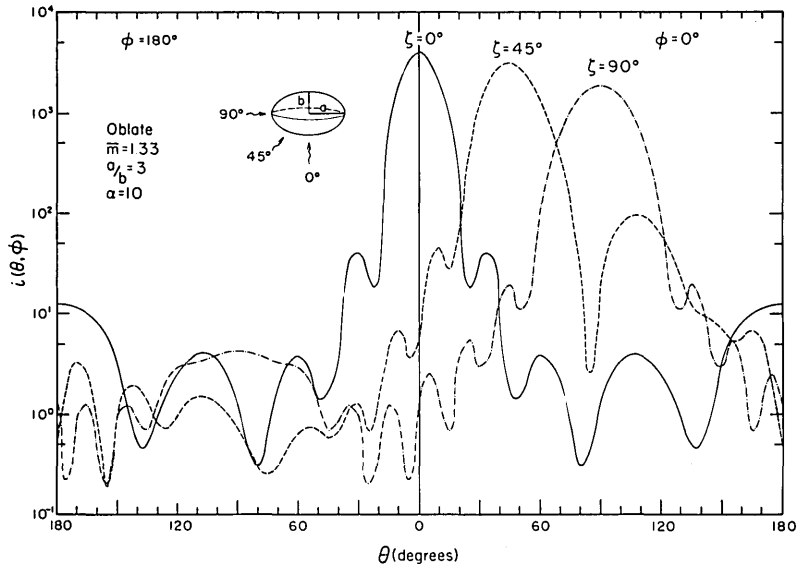

Fig. 13. Angular distribution of the intensity functions $i(\theta,\phi)$ for unpolarized incident light as a function of the zenith angle θ on the incidence plane ($\phi = 0° - 180°$) for the oblate spheroid with $\tilde{m} = 1.33$, $a/b = 3$, and $\alpha = 10$ at incidence angles $\zeta = 0°$, 45°, and 90°.

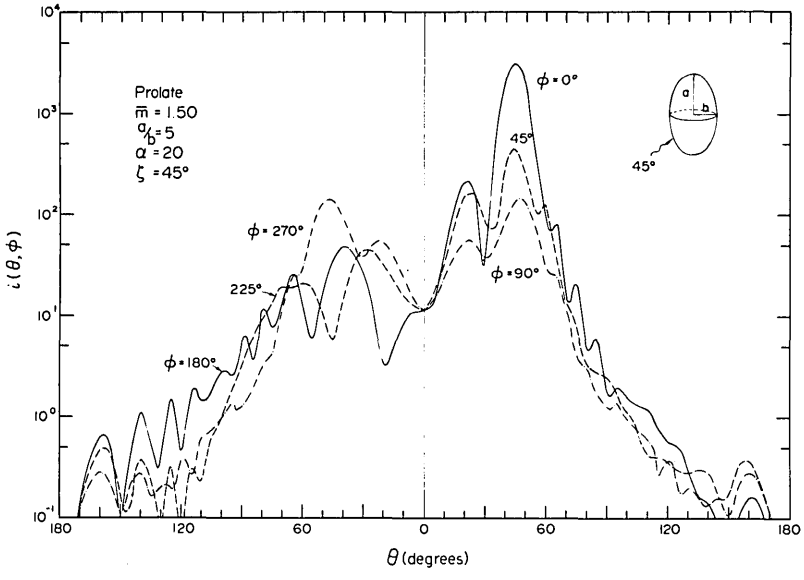

Fig. 14. Angular distribution of the intensity functions $i(\theta,\phi)$ for unpolarized incidence light for the prolate spheroid with $\tilde{m} = 1.50$, $a/b = 5$, and $\alpha = 20$ at $\zeta = 45°$. The figure shows, as a function of the zenith angle θ, the distribution patterns in three scattering planes through the z axis: one parallel to the incidence plane ($\phi = 0°$ and 180°), one inclining from it by an angle 45° ($\phi = 45°$ and 225°), and one normal to it ($\phi = 90°$ and 270°).

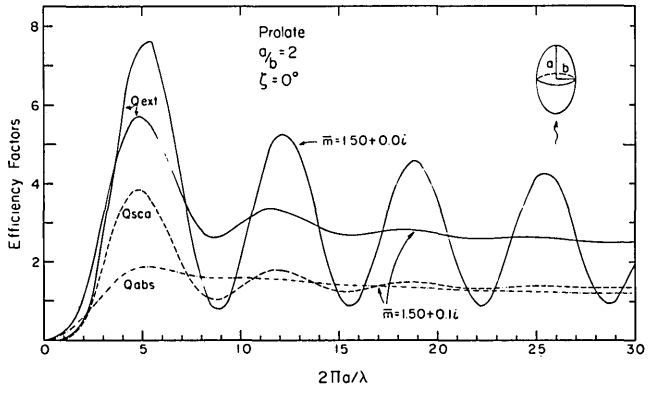

Fig. 15. Efficiency factors for extinction Q_{ext}, scattering Q_{sca}, and absorption Q_{abs} at $\zeta = 0°$ as a function of the size parameter $2\pi a/\lambda$ for absorbing prolate spheroids with $\tilde{m} = 1.50 + 0.1i$ and $a/b = 2$. The extinction efficiency factors for nonabsorbing prolate spheroids with $\tilde{m} = 1.50 + 0.0i$ are also shown.

180°), one inclining from it by an angle 45° ($\phi = 45°$ and 225°), and one normal to it ($\phi = 90°$ and 270°). The intensity functions have maxima in the narrow angle regions around $\theta = 45°$ in each plane, and they decrease rapidly outside the maxima, where, in addition, the intensities in the different planes are of similar magnitude. Note particularly that radiation is hardly scattered in the negative z-axis direction ($\theta = 180°$). At $\zeta = 90°$ (without a figure) the scattered intensity is confined to a narrow angle region around $\theta = 90°$ in every ϕ plane, and its minimum is on the z axis. Thus most radiation scattered by a large slender prolate spheroid at oblique incidence is confined to a narrow angle region surrounding the surface of the cone with an apical angle of $2 \cdot \zeta$ with its axis coincident with the z axis. It is noteworthy that scattering by long prolate spheroids at oblique incidence resembles scattering by infinite circular cylinders. The scattered radiation from an infinitely long cylinder is confined exactly to the surface of the cone with apical angle $2 \cdot \zeta$.[24,32]

VII. Scattering Properties of Absorbing Spheroids

Figure 15 shows the efficiency factors for extinction, scattering, and absorption of absorbing prolate spheroids with $\tilde{m} = 1.50 + 0.1i$ and $a/b = 2$ at parallel incidence $\zeta = 0°$ as a function of the size parameter α. In the figure, the extinction (or scattering) efficiency factors of nonabsorbing prolate spheroids with real refractive index $\tilde{m} = 1.50 + 0.0i$ are also shown. The effects of absorption on the efficiency factors are similar to the effects that are observed for absorbing spheres[21,24,31]: for example, damping of the oscillations of the efficiency curves, shifts of the maxima of the extinction curves to smaller α, and higher extinction efficiency for absorbing spheroids at small sizes $\alpha \lesssim 3.5$. The efficiency factors for scattering Q_{sca} and absorption Q_{abs} approach the geometrical optics limit of unity as size α increases; thus the extinction efficiency factor Q_{ext} converges to the limiting value 2 with diminishing oscillations around that value.

Figure 16 is a comparison of the angular distribution of the intensity functions for scattering by a lossless prolate spheroid ($\tilde{m} = 1.50 + 0.0i$) with the curve for the same prolate spheroid with absorption ($\tilde{m} = 1.50 + 0.1i$). The intensity functions $i_1(\theta)$ at parallel incidence are plotted against θ for prolate spheroids with $a/b = 2$ and $\alpha = 9$. The component $i_1(\theta)$ perpendicular to the scattering plane is more highly structured than the parallel component. The absorption causes a reduction of scattered intensity over almost the entire range of angles, except the forwardscattering peak and a damping of the oscillations. The reduction is much more noticeable in the backscattering, as also shown in Fig. 17.

Figure 17 illustrates the forwardscattering and backscattering intensity functions $i(0°)$ and $i(180°)$ for parallel incidence as a function of the size parameter α for absorbing and nonabsorbing prolate spheroids with $a/b = 2$. The intensity functions $i(0°)$ and $i(180°)$ of the nonabsorbing spheroids ($\tilde{m} = 1.50 + 0.0i$) oscillate regularly with fairly large amplitudes due to the inter-

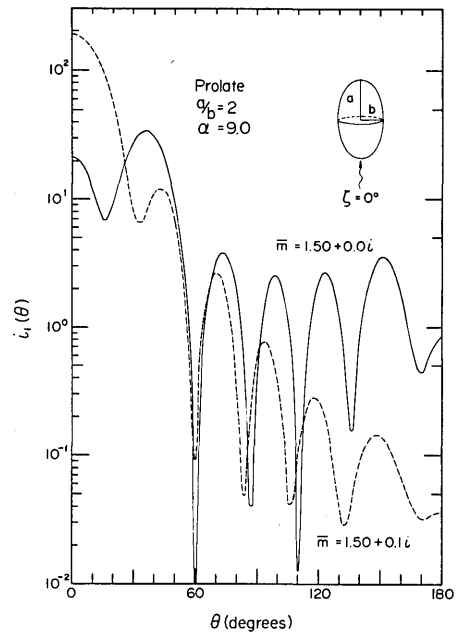

Fig. 16. Angular distribution of the intensity function $i_1(\theta)$ at parallel incidence of the TE mode polarization wave as a function of the zenith angle θ for absorbing ($\tilde{m} = 1.50 + 0.1i$) and nonabsorbing ($\tilde{m} = 1.50 + 0.0i$) prolate spheroids with $a/b = 2$ and $\alpha = 9$.

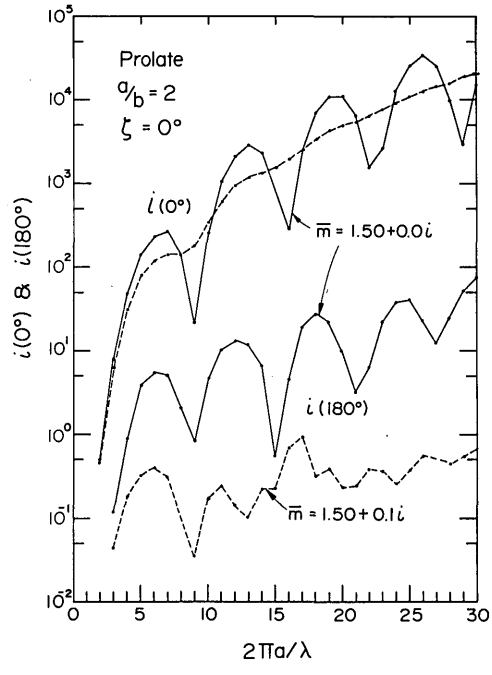

Fig. 17. Intensity functions for forwardscattering $i(0°)$ and backscattering $i(180°)$ at parallel incidence as a function of the size parameter $2\pi a/\lambda$ for absorbing ($\tilde{m} = 1.50 + 0.1i$) and nonabsorbing ($\tilde{m} = 1.50 + 0.0i$) prolate spheroids with $a/b = 2$.

ference effects mentioned before. For the absorbing prolates with $\tilde{m} = 1.50 + 0.1i$, the oscillation of the intensity functions $i(0°)$ is almost damped out, and the intensity functions take approximately the mean value of the oscillating functions of the nonabsorbing prolate spheroids. The backscattering intensity functions of the absorbing prolate spheroids are reduced by more than 1 order of magnitude, and they fluctuate rather irregularly except for the first maximum. This is because of the decrease of transmitted light through the spheroids due to absorption and, in turn, the decrease of interference effects.

One particularly interesting feature of the scattering behavior shown in Fig. 16 is the larger forwardscattering intensity of the absorbing prolate spheroid than that of the nonabsorbing one, by about 1 order of magnitude, together with a relatively high peak at $\theta = 35°$ on the curve of the nonabsorbing prolate spheroid. Such a characteristic peak is seldom observed in scattering by spheres. Barber and Yeh[1] first found this peak in the scattering by the prolate spheroid with $\tilde{m} = 2.236$, $a/b = 3$, and $\alpha = 7.114$, and they attributed its origin to specular reflection off the leading edge of the spheroid. With the aid of Fig. 17, however, we can easily understand that the cause of the low forwardscattering and the high peak at $\theta = 35°$ on the curve of the nonabsorbing prolate spheroid is due to unfavorable interference of diffracted and transmitted light at the forwardscattering direction rather than because of specular reflection. In the calculation of scattering by the slender prolate spheroids with $\tilde{m} = 1.50$ at parallel incidence, we found many such peaks, for example, at $11.0 \leq \alpha \leq 12.0$ for $a/b = 3$, $13.0 \leq \alpha \leq 14.0$, $16.5 \leq \alpha \leq 17.0$, and $24.0 \leq \alpha \leq 25.0$ for $a/b = 4$, and $14.5 \leq \alpha \leq 15.0$ and $19.0 \leq \alpha \leq 20.0$ for $a/b = 5$. Near these size parameters, the scattering efficiency factors and the forwardscattering intensity functions have minima (see Figs. 3 and 10). In the case of spheres, the amplitude of oscillations in the forwardscattering intensity due to interference effects is too small to reduce the forwardscattering intensity lower than the next maximum (Fig. 9).

VIII. Concluding Remarks

The light scattering characteristics of spheroidal particles have been evaluated by the scattering theory we developed for a homogeneous isotropic spheroid. The method has been shown to be quite suitable for computing the scattering quantities of spheroidal particles of fairly large sizes, up to $\alpha \sim 30$. Application of the method to still larger spheroids is at present limited by computational difficulties of the spheroidal wave functions and the infinite series for the solutions discussed in Sec. III.

The dependence of scattering properties on the particle size, shape, refractive index, and orientation has been investigated and physically explained. Relative contributions of the interference effects, surface wave effects, and edge phenomena have been discussed qualitatively. Further study remains to be done with fuller calculations planned for the future.

The scattering properties of the spheroidal particles deviate gradually from those of spheres with an increase of the shape parameter a/b, and, for $a/b \gtrsim 2$, they are already greatly different from those of spheres. The scattering by prolate and oblate spheroids at parallel incidence ($\zeta = 0°$) yields the extremes of the scattering characteristics. The prolate spheroids at $\zeta = 0°$ have steep and high resonance maxima in the scattering efficiency factors and broad and low forwardscattering peaks in the intensity functions except at the sizes of the first maximum of the scattering efficiency factors; on the other hand, the oblate spheroids at $\zeta = 0°$ have broad and low resonance maxima and sharp and high forwardscattering peaks. With the increase of ζ, the scattering properties of the prolate spheroids, except for the magnitude, approach those of the oblate ones at $\zeta = 0°$ and vice versa.

This type of study of the scattering properties of spheroidal particles is important in its own right and also useful for understanding the scattering by other nonspherical particles. A survey of the angular distribution profiles of the intensity functions and the degree of polarization will provide much valuable information on the particle parameters and orientations of nonspherical particles and will be helpful in the determination of those parameters by means of light scattering measurements.

I thank J. E. Hansen for useful discussions and for his hospitality at the Institute for Space Studies. I also thank V. Gurdus for his assistance in numerical computation of the spheroidal wave functions. I extend my appreciation to G. Yamamoto and M. Tanaka for their encouragement. During the course of this research, I held a NAS-NRC Postdoctoral Research Associateship supported by NASA, and I was on leave from Geophysical Institute, Tohoku University, Japan.

References

1. P. W. Barber and C. Yeh, Appl. Opt. **14**, 2864 (1975).
2. P. W. Barber, IEEE Trans. Microwave Theory Tech. **MTT-25**, 373 (1977).
3. P. W. Barber and D. S. Wang, Appl. Opt. **17**, 797 (1978).
4. A. R. Holt, N. K. Uzunoglu, and B. G. Evans, IEEE Trans. Antennas Propag. **Ap-26**, 706 (1978).
5. N. K. Uzunoglu, B. G. Evans, and A. R. Holt, Electron. Lett. **12**, 312 (1976).
6. N. K. Uzunoglu and A. R. Holt, J. Phys. A: Math. Gen. **10**, 413 (1977).
7. H. Weil and C-M. Chu, Appl. Opt. **15**, 1832 (1976).
8. N. K. Uzunoglu, N. G. Alexopoulos, and J. G. Fikioris, J. Opt. Soc. Am. **68**, 194 (1978).
9. T. B. A. Senior and H. Weil, Appl. Opt. **16**, 2979 (1977).
10. A. Nelson and L. Eyges, J. Opt. Soc. Am. **66**, 254 (1976).
11. S. Asano and G. Yamamoto, Appl. Opt. **14**, 29 (1975).
12. C. Flammer, *Spheroidal Wave Functions* (Stanford U.P., Stanford, Calif., 1957).
13. M. M. Stucky and L. L. Layton, Applied Mathematics Laboratory, Department of the Navy Report 164, Washington, D.C. (1964).
14. C. Chang and C. Yeh, USCEE Report 166, Department of Electrical Engineering, U. Southern Calif., Los Angeles (1966).
15. S. Hanish, C. Shely, and R. V. Baier, Naval Research Laboratory Report 6472, Washington D.C. (1966).
16. S. Hanish, R. V. Baier, W. H. Buckler, and B. K. Carmichael, Naval Research Laboratory Report 6502, Washington D.C. (1967).

17. S. Hanish, R. V. Baier, W. H. Buckler, and B. K. Carmichael, Naval Research Laboratory Report 6543, Washington, D.C. (1967).
18. B. P. Sinha and R. H. MacPhie, J. Math. Phys. **16,** 2378 (1975).
19. C. J. Bouwkamp, J. Math. Phys. (Cambridge, Mass.) **26,** 79 (1947).
20. D. B. Hodge, J. Math. Phys. **11,** 2308 (1970).
21. H. C. van de Hulst, *Light Scattering by Small Particles* (Wiley, New York, 1957), pp. 172–179 and 342–364.
22. A. C. Lind and J. M. Greenberg, J. Appl. Phys. **37,** 3195 (1966).
23. A. C. Lind, R. T. Wang, and J. M. Greenberg, Appl. Opt. **4,** 1555 (1965).
24. M. Kerker, *The Scattering of Light* (Academic, New York, 1969).
25. H. C. Bryant and A. J. Cox, J. Opt. Soc. Am. **56,** 1529 (1966).
26. T. S. Fahlen and H. C. Bryant, J. Opt. Soc. Am. **58,** 304 (1968).
27. V. Khare and H. M. Nussenzveig, Phys. Rev. Lett. **38,** 1279 (1977).
28. P. Chýlek, J. Opt. Soc. Am. **66,** 285 (1976).
29. S. T. Shipley and J. A. Weinman, J. Opt. Soc. Am. **68,** 130 (1978).
30. P. Chýlek, J. Opt. Soc. Am. **67,** 175 (1977).
31. J. E. Hansen and L. D. Travis, Space Sci. Rev. **16,** 527 (1974).
32. K.-N. Liou, Appl. Opt. **11,** 667 (1972).